

Cite this: DOI: 10.1039/xxxxxxxxxx

Ground State Cooling and Transport of Single Atoms for Ultracold Molecular Assembly

L. R. Liu,^{abc} J. D. Hood,^{abc} Y. Yu,^{abc} J. T. Zhang,^{abc} K. Wang,^{abc} Y.-W. Lin,^{abc} T. Rosenband,^b and K.-K. Ni^{*abc}

Received Date

Accepted Date

DOI: 10.1039/xxxxxxxxxx

We demonstrate full quantum state control of two species of single atoms using optical tweezers. Our demonstration includes 3D ground-state cooling of a single atom (Cs) in an optical tweezer, transport by several microns with minimal heating, and merge with a single Na atom in an initially separate optical tweezer. Subsequently, both atoms occupy the simultaneous motional ground state with 61(4)% probability. This realizes a sample of exactly two co-trapped atoms near the phase-space-density limit of one, and allows for efficient photo-association of Na and Cs into the vibrational ground state of the electronically excited $c^3\Sigma^+$ potential. The photo-association rate of atoms in their relative motional ground state is enhanced by three orders of magnitude compared to that of thermal atoms. The results are key steps toward coherent spectroscopy and creation of single ultracold molecules with full quantum state control, for future exploration of quantum simulation and quantum information processing.

1 Introduction

Building up complex many-body systems from simpler, well-understood constituents is a promising approach toward understanding and controlling quantum mechanical behavior. Using ultracold molecules as building blocks would offer several prospects to explore both chemistry and physics at their quantum interface.

First, reactant molecules prepared in a pure internal and motional quantum state would allow isolation of single chemical reaction channels¹. Second, the rich molecular internal structure and dipole-dipole interactions would enable quantum simulation of novel quantum many-body phases². Third, single trapped neutral molecules constitute promising qubits for quantum information processing^{3–5}. These prospects hinge on the precise generation and control of ultracold molecules, whose internal and motional quantum states are well defined. Many approaches for trapping and cooling molecules to ultracold temper-

atures are being pursued^{6–16}. Recent highlights include rapid progress made with laser cooling of molecules^{17–20}, the creation of quantum degenerate gases of fermionic KRb²¹, assembling single molecules²² and loading single molecules into an optical tweezer array²³. Bulk samples of ultracold molecules have already proven a versatile platform, enabling the study of ultracold chemistry²⁴ and quantum spin models²⁵. In addition, strongly interacting phenomena can be explored with a lower entropy gas and with single molecule addressability²⁶. We aim to realize both of these capabilities directly by gaining single particle control of molecules without relying on collisions for cooling²⁷.

In this paper, we outline the steps to leverage techniques in optical single atom manipulation^{28–33} to assemble individual molecules²² while maintaining quantum coherence. Furthermore, we experimentally demonstrate full quantum state control including cooling, transport, and merging of two different single atoms, and show thousand-fold enhanced single molecule photo-association rate compared to previous work²².

^a Department of Chemistry and Chemical Biology, Harvard University, Cambridge, Massachusetts, 02138, USA.

^b Department of Physics, Harvard University, Cambridge, Massachusetts, 02138, USA.

^c Harvard-MIT Center for Ultracold Atoms, Cambridge, Massachusetts, 02138, USA.

* E-mail: ni@chemistry.harvard.edu

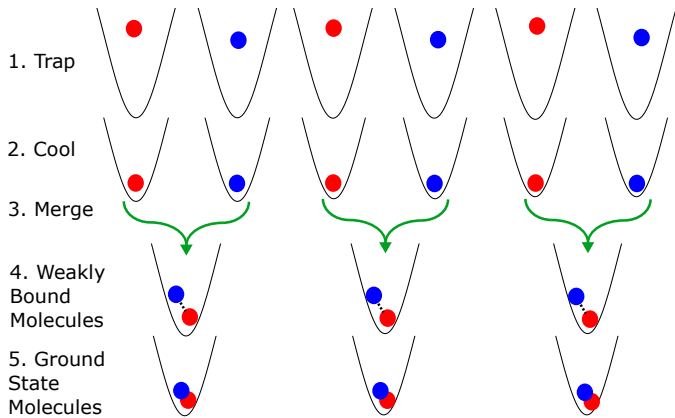


Fig. 1 Step-by-step procedure for the “ultracold molecular assembler.” 1. Trap single atoms in adjacent optical tweezers. 2. Cool atoms into motional ground state. 3. Merge pair of tweezers into one. 4. Convert atom pairs into weakly-bound molecules. 5. Perform coherent internal state transfer to bring weakly-bound molecules to the rovibronic ground state. Three parallel assembly sequences are shown to indicate scalability.

2 Ultracold molecular assembly steps

To assemble single ultracold molecules coherently, we envision an “ultracold molecular assembler” (Fig. 1) that relies on high fidelity internal and external quantum state control of atoms and molecules. The approach is generally applicable to a variety of species. We choose the diatomic molecule sodium cesium (NaCs) due to its large molecular fixed-frame dipole moment (4.6 Debye)^{34,35} and extensive available spectroscopy^{36–38}. For future ultracold chemical reaction studies, NaCs molecules prepared in different internal states offer distinct energetic pathways to participate in chemical reactions that could be switched on and off^{39,40}.

The first step of molecule production (Fig. 1) is to prepare laser-cooled Na and Cs atoms in overlapped magneto-optical traps (MOTs). Single atoms are loaded stochastically from the MOT into spatially-separate tightly-focused optical tweezer traps²⁸. A combination of blue-detuned light assisted collisions⁴¹ and real-time rearrangement^{42,43} could improve the initial atom filling fraction.

A schematic of the apparatus is shown in Fig. 2. As in our previous work²², we generate two tweezer traps at different wavelengths for quasi-independent manipulation of Na and Cs atoms. One of the beams is steerable, so that initially separate tweezer traps can be merged.

Single-atom fluorescence images confirm simultaneous trapping of single Na and Cs atoms side-by-side as shown in Fig. 2.

For efficient conversion into a molecule, the atoms must be trapped in the same tweezer with small spatial wave-

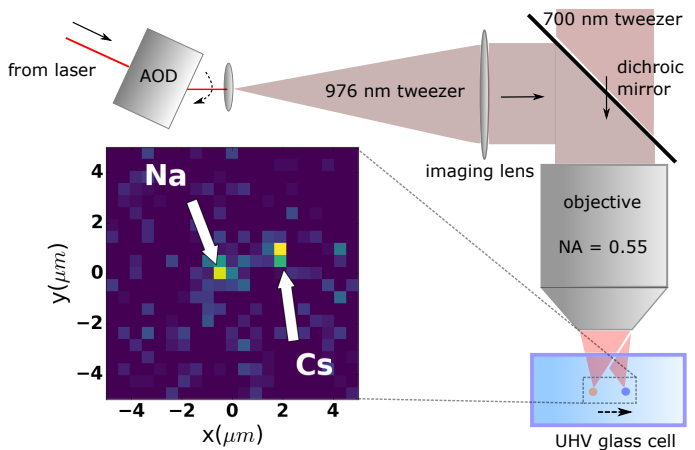


Fig. 2 Single atom trapping and transport. Two neighboring optical tweezers at 976 nm and 700 nm trap a single Cs (blue) and Na (orange) atom in the vacuum chamber. Both tweezer beams are combined on a dichroic mirror and focussed by an objective. The 976 nm tweezer can be moved in the focal plane by changing the drive frequency of an upstream acousto-optic deflector (AOD). Inset: Experimental false-color single-shot fluorescence image of single Na and Cs atoms in adjacent tweezers.

functions. The second experimental step (Fig. 1) minimizes wavefunction-spread by cooling atoms into their motional ground state via 3D Raman sideband cooling (RSC), a technique first demonstrated with single ions⁴⁴ and more recently with single neutral atoms^{30,31,45}.

The two tweezers are then merged (Fig. 1) in order to initialize the Na and Cs atoms in a motional quantum state with large spatial overlap. In a quadratic potential, such as the center of an optical tweezer, two particles interacting via a delta-function potential can be recast into relative and center-of-mass coordinates⁴⁶. Two atoms prepared in their respective motional quantum ground states can then be viewed as being in a single relative motional state.

After cooling, the atoms’ zero-point wavefunction spread exceeds a typical molecular bond length by two or three orders of magnitude, making efficient conversion challenging.

To overcome technical difficulties associated with bridging two quantum states with a large energy difference but small wavefunction overlap, we plan to use two steps (labeled 4. and 5. in Fig. 1). A sodium and a cesium atom in the same tweezer will be first associated into the most weakly bound molecular state by a coherent two-photon Raman pulse^{27,47,48} or through a Fano-Feshbach molecule field ramp⁴⁹. Subsequently, the weakly-bound molecule will be transferred into the rotational, vibrational, and electronic (rovibronic) ground state by stimulated Raman adiabatic passage⁵⁰.

In the following sections, we experimentally detail RSC of a single Cs atom and demonstrate simultaneous ground state cooling, transport, and merging of single Na and Cs atoms, all in a two-species setup. Finally, we photo-associate two single atoms in the same tweezer to the deeply bound $v' = 0$ vibrational ground-state of the NaCs $c^3\Sigma^+$ potential.

3 Controlling the Quantized Motion of Atoms

Using a standard MOT followed by polarization gradient cooling (PGC), it is possible to cool the motion of single Cs or Na atoms to an average of tens of quanta in a tight tweezer trap. To further cool the atoms into the lowest motional state, we operate in the resolved sideband regime where the linewidth of the cooling transition is less than the trap frequency (10-100's of kHz). We have previously demonstrated ground-state cooling of single Na³³. Here, we demonstrate 3D RSC of a single Cs atom in an optical tweezer. To our knowledge, we report the highest 3D ground-state probability for single atoms in tweezers to date.

The RSC sequence consists of two steps: a coherent two-photon Raman transition that connects two internal states while removing a motional quantum, and an optical pumping (OP) step that re-initializes the internal state of the atom. The two steps are repeated until the atom reaches the motional ground state.

In our scheme (Fig. 3), the Raman transition occurs between Cs ground-state hyperfine levels $|F = 4, m_F = -4; n\rangle$ and $|3, -3; n-1\rangle$, which are about 9.2 GHz apart. Here, n is the motional quantum number. The transition is driven by two phase-locked diode lasers, “F3” and “F4”, both red-detuned by $\Delta = 2\pi \times 44$ GHz from the Cs D_2 line at 852 nm, and with Rabi rates Ω_{F3} and Ω_{F4} , respectively. The tweezer has a power of 14.3 mW and beam waist of 0.84 μm . To achieve motional coupling, the laser beams are arranged as shown in the inset of Fig. 3A. This configuration yields substantial two-photon momentum transfer, $\vec{\Delta k} = \vec{k}_{F4(i)} - \vec{k}_{F3}$, while the energy difference associated with the hyperfine level and motional state change is supplied by their relative detuning, δ . This resonance condition is maintained for all relevant motional states, n .

The atom is initially prepared in $|4, -4\rangle$ by OP (independently of the motional state, n). For this, we use σ^- -polarized beams resonant with $|4, -3\rangle \rightarrow |4', -4\rangle$ and $|3, -3\rangle \rightarrow |4', -4\rangle$ transitions, where the primed levels denote sub levels of the $6P_{3/2}$ manifold of Cs. During the first step of RSC, a Raman π -pulse drives the transition $|4, -4; n\rangle \rightarrow |3, -3; n-1\rangle$. Subsequently, OP pumps the atom to $|4, -4; n-1\rangle$. OP preserves the motional state with high

probability. Thus, in each RSC cycle, n decreases on average. The process repeats until the atom reaches the dark state $|4, -4; 0\rangle$, thereby deterministically preparing the internal and the motional quantum state of the atom.

We switch between the three Raman F4(i) directions in the sequence $i = 3, 1, 2, 1$ to cool the atomic motion along all three axes of the tweezer. The tweezer potential has a cigar shape with two near-degenerate, tightly confined radial directions and a loosely confined axial (along the tweezer beam propagation) direction.

The linewidth of the Raman transition is Fourier broadened due to the finite duration of a π -pulse, which is inversely related to the peak effective Raman Rabi rate $\Omega_R = \Omega_{F3}\Omega_{F4}/2\Delta = 2\pi \times 33\text{kHz}$ ($2\pi \times 7\text{kHz}$) for radial (axial) trap axes. The smaller energy splitting of the axial motion necessitates a smaller Raman coupling along that direction. An 8.6 G magnetic field is applied throughout RSC along the OP propagation direction to define the quantization axis.

All Raman pulses in this experiment for cooling and spectroscopy use a Blackman window temporal intensity profile to reduce off-resonant excitation of the carrier. The starting temperature of $9.2\mu\text{K}$, corresponding to a mean axial motional quantum number $\bar{n}_a = 9$, leads to non-negligible occupation of levels up to $n_a \approx 40$.

Due to the \sqrt{n} scaling of sideband transition strengths⁵¹, it was necessary to “sweep” the Raman pulse durations in descending order starting from $n_a^{init} = 41$. Furthermore, to overcome decoherence, which reduces the transfer fidelity of each pulse, we repeat the sweep, but each time with a smaller $n_a^{init} = \{41, 31, 16, 11, 6\}$. The entire process takes ≈ 100 ms.

We characterize two cooling experiments in Fig. 3(B): (1) sub-optimal cooling was used with slightly off-resonant $\delta \neq \omega_{trap}$ to reveal the location of the $\Delta n = -1$ sidebands. (2) optimal cooling is obtained by setting $\delta = \omega_{trap}$, as determined by the sideband locations in (1).

To characterize the cooling performance, we use sideband thermometry⁴⁴. Following RSC, we measure the ratio of $\Delta n = -1$ and $\Delta n = +1$ Raman sideband transition heights. A successful transition changes the state from $|4, -4\rangle$ to $|3, -3\rangle$ and is revealed by state selective imaging: light that is resonant with the cycling $|4, -4\rangle \rightarrow |5', -5\rangle$ transition ejects only $|4, -4\rangle$ atoms. The remaining atoms in $|3, -3\rangle$ are then imaged. We obtain the average occupation number \bar{n} from the ratio of sideband heights via $I_{-1}/I_{+1} = \frac{\bar{n}}{\bar{n}+1}$. By assuming a thermal distribution, we extract a temperature and a ground state probability along each axis. The product of the ground state probabilities in all three dimensions gives the 3D ground state probability P_0^{3D} .

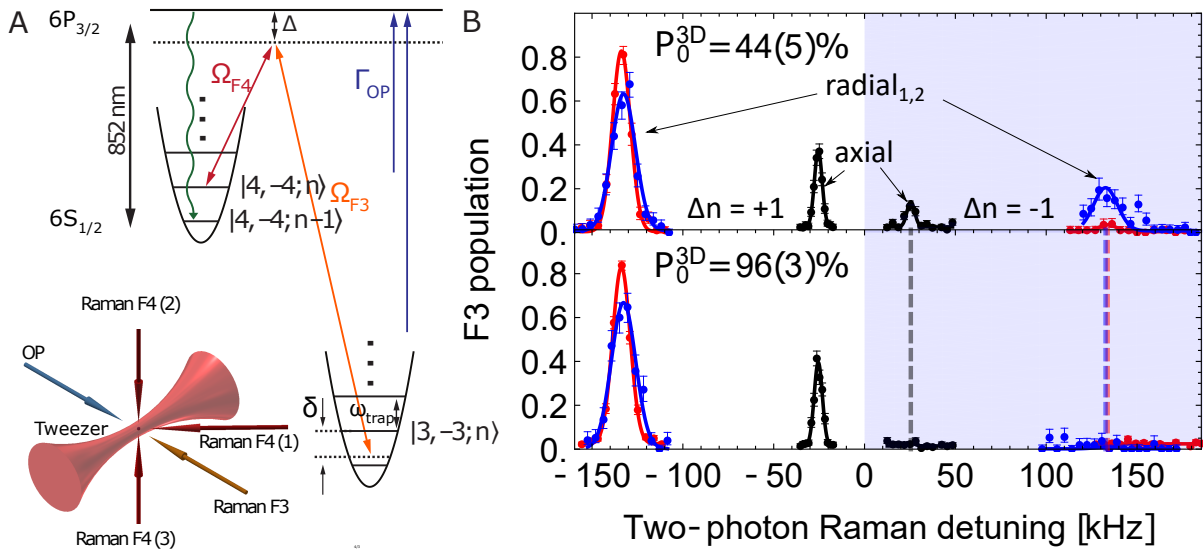


Fig. 3 3D motional control of a single Cs atom. (A) Level scheme for Cs RSC. F3 and F4 Raman beams coherently couple adjacent motional states to reduce motional energy, while optical pumping provides the dissipation needed for cooling. **[Inset] Directions of laser beams.** Switching Raman F4 beam directions allows addressing motion in all 3 dimensions. **(B) 3D sideband thermometry for Cs after RSC.** Black, blue, and red spectral peaks in the unshaded (shaded) region correspond to $\Delta n = +1(-1)$ sidebands for the axial and two radial directions, respectively. Above: Spectra after sub-optimal RSC reveals the $\Delta n = -1$ sidebands, and hence the motional frequencies. The 3D ground state population is $P_0^{3D} = 44(5)\%$. Below: Spectra after cooling with optimized motional frequencies, yielding $P_0^{3D} \geq 96(3)\%$.

$\{\bar{n}_a, \bar{n}_{r1}, \bar{n}_{r2}\} = \{0.03(3), 0.00(1), 0.01(1)\}$, corresponding to $P_0^{3D} \geq 96(3)\%$ for optimal cooling.

The signal contrast in Fig 3B does not reach unity due to the $\approx 300 \mu\text{s}$ coherence time for driving motional sideband transitions. Furthermore, different pulse durations were used on the two radial axes, leading to a further difference in contrast. However, the sideband *ratios*, used to extract the final ground state population, are unaffected.

A final consideration is that any wait time between the end of RSC and molecule formation needs to be minimized because the atoms can be heated by off-resonantly scattering photons from their respective tweezers. This occurs at a rate of $\Delta n_a \approx 0.3 \text{ Hz}$. To avoid unnecessary waiting, we perform the Na and Cs RSC sequences concurrently so that they end at the same time. We have verified experimentally that RSC of one species does not affect the atom of the other species.

4 Preparing both Na and Cs in the ground state of the same tweezer

While merging two separately confined identical ground-state atoms into one potential well requires delicate quantum tunneling⁵², merging different atomic species is more straightforward. Due to their different atomic polarizability as a function of wavelength, two different color optical tweezers allow the two atoms to be manipulated quasi-independently²².

One tweezer beam at a wavelength of 700 nm confines Na at the intensity maximum while repelling Cs. A second tweezer beam at a wavelength of 976 nm strongly confines Cs while weakly attracting Na. As shown in Fig. 4A, translation of the 976 nm beam to overlap the 700 nm beam, followed by gradual turn-off of the 700 nm beam leaves the two atoms confined in the same tweezer trap, all within 10 ms. The exact trajectory is detailed in the Supplement⁵³.

After running this sequence (in the absence of Na) followed by its time reverse for detection, Raman sideband thermometry on the separated tweezer shows minimal motional excitation of Cs ($\{\Delta \bar{n}_z, \Delta \bar{n}_{r1}\} = \{0.01(5), 0.00(2)\}$) (Fig. 4B).

We further explore different trap powers for merging of Cs and Na atoms into one tweezer. To prevent spin-changing collisions²², we first prepare Na in $|2, 2\rangle$ and Cs in $|4, 4\rangle$. Then, we merge the atoms and measure the joint axial ground state fraction $P_{n_z=0}^{\text{Na}} \times P_{n_z=0}^{\text{Cs}}$ as a function of beam powers (Fig. 4C). We identify three issues that can cause excess heating during the merge and require careful beam-power selection to overcome:

1. The 976 nm beam can make Na spill from the 700 nm tweezer and gain kinetic energy. This limits the ratio $P_{700\text{nm}}/P_{976\text{nm}}$ to be above 0.37, indicated by the right shaded triangle in Fig. 4C, and the left panel at 5.7 ms in Fig. 4A.

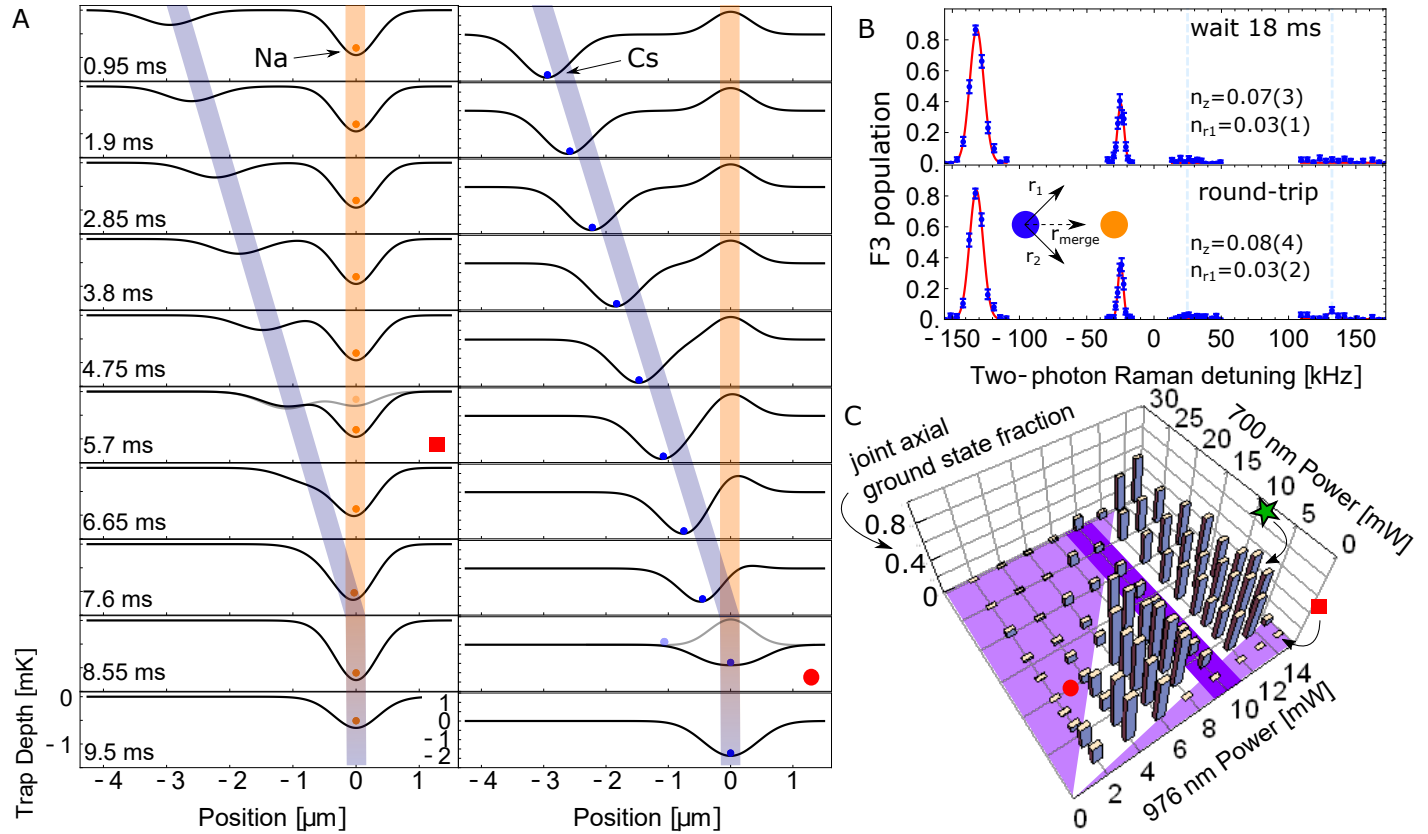


Fig. 4 Merging atoms in two tweezers while maintaining quantum motional states. (A) Radial cuts of optical potential experienced by Na and Cs during the merge time sequence. Blue and orange lines show paths of the 976 nm and 700 nm tweezers, respectively. The 976 nm tweezer containing Cs is translated by $2.95 \mu\text{m}$ in 7.6 ms until it overlaps with the 700 nm tweezer. Then, the 700 nm tweezer power is linearly ramped from 48 mW to 0 mW in 1.5 ms, followed by a $50 \mu\text{s}$ wait. Lighter potential in the left 5.7 ms panel (marked by red square) shows the scenario for tweezer powers leading to spilling of Na. Lighter potential in the 8.55 ms panel (marked by red circle) shows the scenario for tweezer powers giving rise to anti-trapping for Cs. **(B) Raman sideband spectroscopy to characterize heating associated with atom transport.** Top: A control experiment holding the atoms stationary for 18 ms. Bottom: After the *round-trip* merge sequence (the sequence shown in (A) followed by its time reverse) Dashed blue lines indicate expected position of $\Delta n = -1$ sidebands. The *round-trip* sequence causes minimal heating. Inset: Coordinates of the transport direction vs a thermometry axis. Blue and orange circle represent 976 nm and 700 nm tweezers respectively. **(C) Na+Cs joint axial ground state fraction after round-trip merge sequence as a function of 700 nm and 976 nm tweezer powers.** The lower triangle corresponds to spilling of Na. Red square is an exemplary point in this regime, whose radial potential is plotted in underlay in the correspondingly marked panel in (A). Upper triangle indicates anti-trapping of Cs. Red circle is an exemplary point, whose potential is plotted in underlay in the correspondingly marked panel in (A). Dark purple stripe shows parametric heating resonance (due to technical imperfection) during transport of Cs. Our usual operating point is indicated by the star.

2. The 700 nm beam can dominate the 976 nm beam and repel Cs from the trap. This limits the power ratio of the beams $P_{700\text{nm}}/P_{976\text{nm}}$ to be below 2.7, indicated by the left shaded triangle in Fig. 4C, and the right panel at 8.55 ms in Fig. 4A.
3. Technical beam-steering imperfections cause a position-depending sinusoidal ripple of the 976 nm tweezer intensity. For beam powers near $P_{976\text{nm}} = 10$ mW at our moving speed, this leads to parametric heating of the Cs axial mode.

We choose powers of $P_{976\text{nm}} = 14.3$ mW and $P_{700\text{nm}} = 7.1$ mW (also used in Fig. 4B) for all subsequent experiments. We characterize with 3D Raman sideband thermometry that we have prepared two atoms in the same tweezer with a phase space density (PSD) of $P_0^{Na} \times P_0^{Cs} = 0.80(3) \times 0.76(4) = 0.61(4)$. In this experiment, lower optical pumping fidelity resulted in a higher initial Cs temperature as compared to Sec. 3.

5 Enhanced Photo-association of Single Molecules

High PSD of trapped Na and Cs enhances the rate of single molecule formation due to increased atom pair density and collision cross section⁵⁴. In our experiment, we probe such an enhancement by the photo-association (PA) rates for transitions from free atoms ($|F = 2, m_F = 2\rangle$ for Na and $|4, 4\rangle$ for Cs) into the deeply-bound $c^3\Sigma_1^+(v' = 0, J' = 2)$ state. Details of the observation are given in Fig. 5. The measured resonance frequency is 288,698.54(6) GHz, where the uncertainty is dominated by the wavemeter inaccuracy of 60 MHz. Our frequency measurement may be compared to an extrapolated value of 288,731 GHz based on the Dunham expansion coefficients³⁶, and 288,670(15) GHz, based on a previous measurement of the $c^3\Sigma_1^+(v' = 0) \leftarrow X^1\Sigma^+(v'' = 9)$ transition⁵⁵ and the calculated binding energy of $X^1\Sigma^+(v'' = 9)$ ⁵⁶. We also measure a $J' = 2 \rightarrow J' = 3$ splitting of 6.6 GHz, giving a rotational constant of 1.1 GHz.

Fig 5C shows resonant PA as a function of PA pulse duration in the “quantum” and the “classical” regimes. For these measurements, the tweezer parameters are identical to those in Section 4 and the “quantum” regime is accessed by the ground-state-cooling and merging steps described in Sections 3 and 4, although technical issues reduced the cooling efficiency. The “classical” regime is accessed via the same merge sequence but without sideband-cooling and has a PSD of 10^{-6} (see Supplement). The PA rate in the classical regime is dominated by a single $1/e$ decay timescale of 53(4) ms, whereas the quantum regime

shows two distinct components with 16(8) μ s and 9(3) ms timescales.

The fast quantum timescale represents a factor of $3(2) \times 10^3$ enhancement in PA rate over the classical case. This factor is compatible with the collision rate formula $\Gamma_{PA}^{max} = \rho \pi v_{rel} / k_{rel}^2$, which predicts a 1.7×10^3 times faster PA rate in the quantum regime⁵³. Here, ρ is the pair density, v_{rel} is the relative velocity, and $\hbar k_{rel}$ is the relative momentum⁵⁴.

PA of molecules occurs when atoms collide while absorbing a resonant photon. Therefore, the PA rate is dictated by the relative motion of the two atoms. Such collisions can be suppressed by an angular momentum barrier. For a spherical trap with separable coordinates, we calculate the Franck-Condon factor for *p*-wave PA transitions to be two orders of magnitudes lower than for *s*-wave transitions, similar to the observed ratio of time scales in the “quantum” regime.

6 Summary and outlook

We present tools for dual species single atom manipulation for the coherent assembly of single ultracold polar molecules.

We have demonstrated trapping of the constituent atoms (Cs and Na) side-by-side in optical tweezers, motional ground-state cooling of Cs to its 3D ground state (96 %), and merging single Cs and Na atoms into the same tweezer while maintaining both atoms in the motional ground state (61 %). Photo-association of the atom pair shows that ground state cooling speeds the production of deeply-bound molecules by three orders of magnitude. This is an important step towards the goal of efficient assembly of single molecules from individual atoms. Furthermore, two atoms prepared in the ground state of the same tweezer are a valuable resource to investigate interactions, collisions, and coherent spectroscopy and creation of molecules.

The number of atom pairs could be scaled up by employing an array of single atom tweezer traps as a starting point^{42,43}, to assemble molecules in parallel. This ultracold molecular assembler features fast cycle time, flexible geometry, individual control and imaging capabilities, and provides an attractive platform for studies of ultracold chemistry, quantum information, and many body physics.

7 Acknowledgments

This work is supported by the Arnold and Mabel Beckman Foundation, as well as the NSF (PHYS-1806595), the AFOSR Young Investigator Program, and the Camille and Henry Dreyfus Foundation. J.T.Z acknowledges support from the NDSEG fellowship.

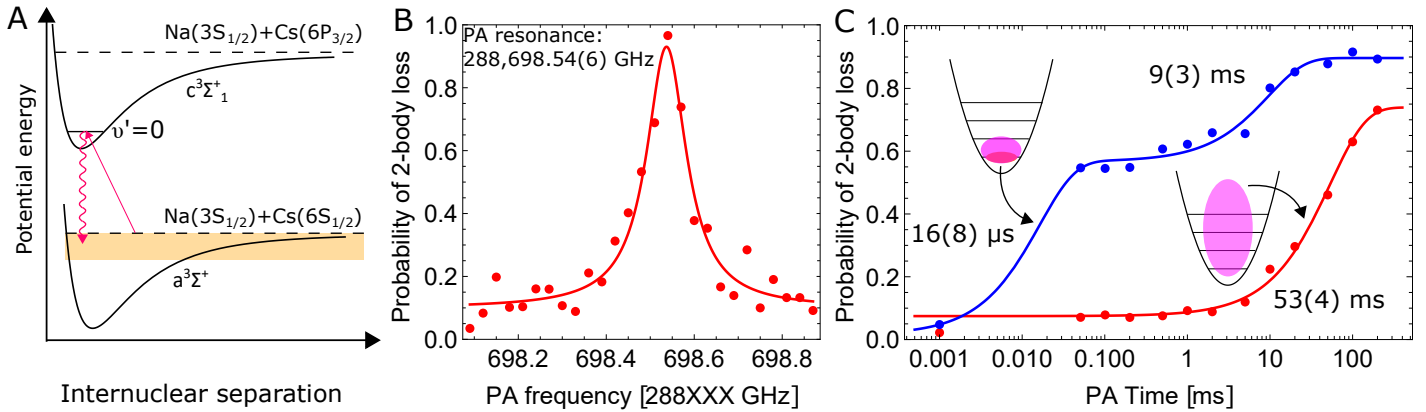


Fig. 5 Enhanced photoassociation (PA) of Na and Cs. (A) Potential energy curves. Both atoms are initially confined by the tweezer potential at the asymptote of the $a^3\Sigma^+$ NaCs molecular ground electronic state. A PA beam (15 mW, σ^+ -polarized, 10 μm radius) excites the pair to the electronic excited $c^3\Sigma_1^+$, which subsequently spontaneously decays into a manifold of vibrational levels (yellow region) in $a^3\Sigma^+$. **(B) PA resonance of the $c^3\Sigma_1^+(v'=0, J'=2) \leftarrow a^3\Sigma^+$ transition.** Shown is the Na + Cs two-body loss probability as a function of the PA frequency for a 75 ms pulse duration. **(C) Time dependence of resonant PA in the quantum (blue) and classical (red) regimes.** The red curve is a single exponential with $1/e$ decay time of 53(4) ms. The blue curve is a sum of two exponentials with decay times of 16(8) μs and 9(3) ms. The distributions of relative motional states for the two cases are indicated schematically.

8 Supplement

8.1 Trajectory of merging two atoms into one tweezer

The speed at which we choose to transport a Cs atom in the 976 nm tweezer and subsequently merge it with the 700 nm tweezer is constrained by two main factors: (1) minimizing heating due to jerk (time-derivative of acceleration) at the endpoints, and (2) avoiding trap depth oscillations at a frequency that could cause parametric heating⁵⁷.

To address (1), we use the so-called “minimum-jerk trajectory”⁵⁸ to transport Cs. It is designed to translate the equilibrium point of a classical harmonic oscillator with minimal motional excitation. The displacement x as a function of time t is given by

$$x(t) = x_{min jerk}(t, d, T) = d \left(10\left(\frac{t}{T}\right)^3 - 15\left(\frac{t}{T}\right)^4 + 6\left(\frac{t}{T}\right)^5 \right)$$

$$x(t) = \begin{cases} x_{min jerk}(t, 2\Delta f, 2\Delta t) & \text{for } 0 \leq t \leq \Delta t \\ \frac{15}{4} \frac{\Delta f}{2\Delta t} & \text{for } \Delta t < t < T - \Delta t \\ x_{min jerk}(t - T + 2\Delta t, 2\Delta f, 2\Delta t) + \alpha T \frac{15}{4} \frac{\Delta f}{2\Delta t} & \text{for } T - \Delta t < t \leq T \end{cases}$$

where $\Delta f = d/(2 + \frac{15}{4} \frac{\alpha}{1-\alpha})$ and $\Delta t = \frac{1}{2}T(1-\alpha)$ are the distance covered and time elapsed, respectively, of the minimum jerk trajectory portion, and α is the fraction of the trajectory that is linear motion and can range from 0 (fully minimum jerk) to 1 (fully linear).

For data in Fig 4B, we use $d = 2.5 \mu\text{m}$, $T = 7.6 \text{ ms}$, and $\alpha = 0$. For the data in Fig 4C, we use $d = 2.95 \mu\text{m}$ and $\alpha = 0.95$. We find the hybrid trajectory is more robust against

where d is the total distance traveled and T is the total move time.

However, the minimum jerk trajectory has a variable moving speed that is problematic for constraint (2). Because the tweezer is transported by sweeping the RF frequency that drives the AOD in Fig. 2, the trap depth oscillations arising from imperfections of the AOD (see Section 8.3) would sweep through a band of frequencies and be more likely to excite a parametric heating resonance.

Therefore, we devise a hybrid trajectory which uses constant velocity in the middle and minimum jerk at the endpoints. Thus, the oscillation frequency is constant for the middle part and the parameters can be more easily chosen to avoid parametric resonances. The displacement as a function of time for the hybrid trajectory is given by

parametric heating.

8.2 Simulating merging of two tweezers

To find the fastest speed at which we can merge single Na and Cs atoms tweezers into the same tweezer, we simulate their time evolution using the split operator method⁵⁹.

The atomic polarizabilities are taken from Table 2 of Ref. 60. The initial and final trap eigenfunctions are cal-

culated with the Fourier Grid method⁶¹. The ground state population at the end of the sequence is given by the squared overlap of the wavefunction following the time evolution with the ground state of the final trap. The accuracy of these simulations is determined by the time step Δt and position grid spacing Δx . The accuracy of the split operator method is then set by $[H, V]\Delta t^2$, where H is the Hamiltonian and V is the potential energy. For the simulation data presented here, we use a time step of $\Delta t = 0.1 \mu\text{s}$ and spatial grid spacing $\Delta x = 1 \text{ nm}$, and have checked that the simulation converges at these values.

The tweezer waist is estimated from scalar Gaussian beam propagation simulation of the input beam (whose waist we can measure), including the effect of the beam clipping on the objective aperture. The simulated electric field intensities along the radial and axial directions are fitted independently to those of a Gaussian beam. We find that doing so gives an input beam that is Gaussian except that the Rayleigh range is scaled by 1.39, to account for aberrations.

For the 976 nm tweezer, for 15 mW measured before a final beam expanding telescope, 9 mm waist input before the objective, the radial and axial waists at the tweezer are $0.844 \mu\text{m}$ and $4.875 \mu\text{m}$ ($\text{zR} = 1.006 \mu\text{m}$) respectively. We match the calculated and measured radial and axial trapping frequencies of 125.7 kHz and 24.1 kHz respectively, by inserting a transmission coefficient $T = 0.27$ by hand. This includes transmission through many optical elements: dichroics, objective, glass cell, and electrode plate surfaces. Similarly, for the 700 nm tweezer, 6.6 mm input waist, 48 mW power before a final beam expanding telescope, $T = 0.36$ gives 530.5 kHz and 92.7 kHz radial and axial trap frequencies, in good agreement with measurements.

By scanning the merge time and calculating the final wavefunction overlap with the motional ground state wavefunction, we find that we can scan more than 10× faster (i.e. $2.95 \mu\text{m}$ in $<1 \text{ ms}$) using a minimum jerk trajectory and still remain in the ground state with $>99.9\%$ probability (see Fig 6), provided there are no technical imperfections.

8.3 Derivation of trap depth oscillation frequency

We use an IntraAction A2D-563AHF3.11 which can deflect the beam in two dimensions. The electro-optic medium is not angle-cut, and forms an acoustic cavity. The amplitude of the intracavity field affects the AOD diffraction efficiency and depends on RF drive frequency. Therefore, as the RF drive frequency is scanned to move the tweezer, the trap depth oscillates, in this case by 1%.

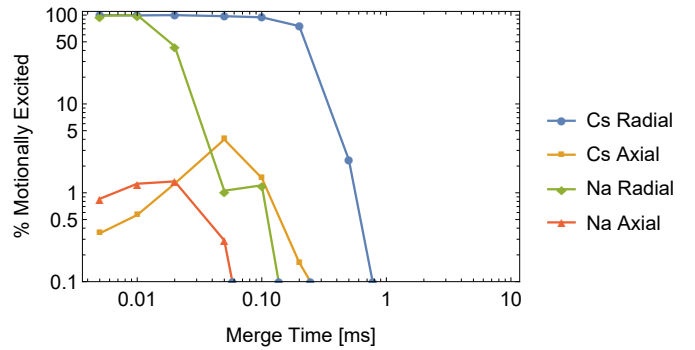


Fig. 6 Minimum merge time. We numerically simulate the motional excitation as a function of merge time with fixed trap depth.

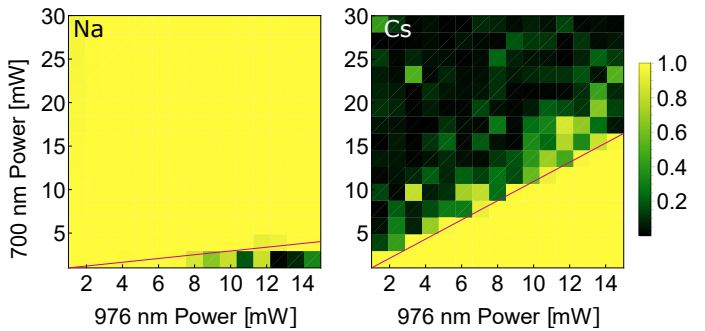


Fig. 7 Simulated 2D tweezer power scan. Numerical simulation of the axial ground state population for Na and Cs following the merge sequence described in Sec. 4. All the fundamental heating mechanisms (delineated by purple lines) are qualitatively reproduced.

By scanning the tweezer position along the merge axis and measuring the period of the intensity fringes, we measure the free spectral range of the acoustic cavity to be $FSR = 97.5 \text{ kHz}$. This is consistent with $FSR = v/2L$ where the length of the acousto-optic crystal $L \approx 2\text{cm}$ and the speed of sound is $v = 3.63 \text{ mm}/\mu\text{s}$.

Scanning the RF drive frequency by 9.44 MHz moves the 976 nm trap $2.95 \mu\text{m}$ in the focal plane.

Therefore, the acoustic cavity causes the trap depth to oscillate at a frequency $v_{move} 9.44 \text{ MHz} / (FSR \times 2.95 \mu\text{m})$, where v_{move} is the speed at which the trap moves. For our hybrid trajectory in Section 4, the trap depth oscillation during the linear part is therefore 9.9 kHz.

8.4 Simulated tweezer power 2D scan

We perform a numerical simulation of the dynamics of merging atoms into one tweezer with different 700 nm and 976 nm tweezer powers. This yields the plots in Fig 7A and B for Na and Cs, respectively. We find that heating regions arising from double-well for Na and anti-trapping of Cs are qualitatively reproduced (discrepancy in the exact

size of the heating regions are attributed to aberrations of the tweezers which cause the actual trap depth to be different than expected).

We observe more overall heating in the experimental data compared to simulation, even in the regions that have no specific heating mechanism. This is likely caused by axial misalignment, which we estimate to be about $1.5 \mu\text{m}$ in this experiment.

8.5 Calculation of phase space density (PSD)

We define $0 < PSD \leq 1$ as the peak occupation of the joint Na and Cs system per quantum state. It characterizes the quantum state purity of the system prior to molecule formation, and therefore how far the atoms are into the quantum regime. Furthermore, the closer PSD is to 1, the more efficiently we expect to form molecules, provided the relative wavefunction does not contain a node at the origin. For a thermal state in a harmonic oscillator, the occupation probability of motional state n in the i -direction is

$$P_i(n) = \bar{n}_i^n / (\bar{n}_i + 1)^{n+1}$$

where $\bar{n}_i = 1/(e^{\hbar\omega_{trap}^i/(k_B T)} - 1)$ is the average occupation number. The ground state $n = 0$ is the most populated quantum state, so the PSD is given by

$$P_x^{Na}(0)P_y^{Na}(0)P_z^{Na}(0)P_x^{Cs}(0)P_y^{Cs}(0)P_z^{Cs}(0)$$

In the classical regime, using $\omega_{trap}^x = 2\pi \times 132 \text{ kHz}$ and $\omega_{trap}^z = 2\pi \times 24 \text{ kHz}$ for Na and $2\pi \times 150 \text{ kHz}$ and $2\pi \times 27 \text{ kHz}$ for Cs, and starting temperatures of $T_{Na} = 42 \mu\text{K}$ and $T_{Cs} = 28 \mu\text{K}$, we obtain $PSD_{classical} = 1.2 \times 10^{-6}$.

8.6 Calculation of PA enhancement

We use the collision rate formula to estimate the maximum PA rate,

$$\Gamma_{PA}^{max} = \rho \pi v_{rel} / k_{rel}^2$$

The enhancement of photo-association rates of atoms prepared in the quantum regime can therefore be explained in terms of two effects which take hold at low temperature: increased ρ due to smaller atomic wavefunction spread and increased collision cross section $\sim 1/k_{rel}^2$ due to longer de Broglie wavelength.

In the classical case ($T_{Na} = 42 \mu\text{K}$ and $T_{Cs} = 28 \mu\text{K}$), thermal bosons in a harmonic potential have a density profile given by

$$n(x, y, z) = \prod_{i=x,y,z} \frac{1}{\sqrt{2\pi\sigma_i^2}} \exp(-i^2/2\sigma_i^2),$$

where $\sigma_i = \sqrt{\frac{k_B T}{m(\omega_{trap}^i)^2}}$, k_B is Boltzmann's constant, T is

the temperature, m is the mass, and $\omega_{trap}^i/(2\pi)$ is the trap frequency in the i -direction. The pair density is given by

$$\rho = \int n_{Na}(x, y, z) n_{Cs}(x, y, z) dx dy dz$$

where $v_{rel} = \sqrt{3k_B(T_{Na}/m_{Na} + T_{Cs}/m_{Cs})}$, $\hbar k = \mu v_{rel}$, and $\mu = m_{Na} m_{Cs} / (m_{Na} + m_{Cs})$. In this case, we find $\rho = 3.1 \times 10^{12} \text{ cm}^{-3}$ and $\Gamma_{PA,th}^{max} = 452 \text{ Hz}$.

For the case of atoms in the absolute ground state, we use

$$\Gamma_{PA,0}^{max} = \rho \pi \sqrt{\sum_{i=x,y,z} (v_{rel}^i / (k_{rel}^i)^2)^2}$$

The probability density of the atom in the trap motional ground state is

$$n(x, y, z) = \prod_{i=x,y,z} \frac{1}{l_{ho}^i \sqrt{\pi}} \exp(-i^2 / (l_{ho}^i)^2)$$

where $l_{ho}^i = \sqrt{\hbar / (m\omega_{trap}^i)}$ is the trap oscillator length in the i -direction. In relative coordinates, the RMS relative momentum in the i -direction is given by $\hbar k_{rel}^i = \sqrt{\hbar\mu\omega_{trap}^i/2}$ and velocity $\mu v_{rel}^i = \hbar k_{rel}^i$. For the cold atoms, $\rho = 3.2 \times 10^{14} \text{ cm}^{-3}$ and $\Gamma_{PA,0}^{max} = 754 \text{ kHz}$.

The ratio of collision rates is then given by $\Gamma_{PA,0}^{max} / \Gamma_{PA,th}^{max} = 1.7 \times 10^3$, which qualitatively explains the enhanced PA rate we measured in Sec. 5.

We note that the use of Γ_{PA}^{max} to estimate the PA enhancement ignores the variation of the Franck-Condon factors over the range of thermally populated motional states in the classical regime. However, we have calculated that the Franck-Condon factors should vary by less than a factor of 5 over the range of relevant motional states.

References

- 1 R. V. Krems, *Physical Chemistry Chemical Physics*, 2008, **10**, 4079.
- 2 M. A. Baranov, M. Dalmonte, G. Pupillo and P. Zoller, *Chemical Reviews*, 2012, **112**, 5012–5061.
- 3 D. DeMille, *Phys. Rev. Lett.*, 2002, **88**, 067901.
- 4 A. Andre, D. DeMille, J. M. Doyle, M. D. Lukin, S. E. Maxwell, P. Rabl, R. J. Schoelkopf and P. Zoller, *Nat. Phys.*, 2006, **2**, 636–642.
- 5 K.-K. Ni, T. Rosenband and D. D. Grimes, *Chem. Sci.*, 2018, **9**, 6830–6838.
- 6 L. D. Carr, D. DeMille, R. V. Krems and J. Ye, *New Journal of Physics*, 2009, **11**, 055049.
- 7 K.-K. Ni, S. Ospelkaus, M. H. G. de Miranda, A. Pe'er, B. Neyenhuis, J. J. Zirbel, S. Kotochigova, P. S. Julienne, D. S. Jin and J. Ye, *Science*, 2008, **322**, 231–235.
- 8 J. G. Danzl, E. Haller, M. Gustavsson, M. J. Mark,

R. Hart, N. Bouloufa, O. Dulieu, H. Ritsch and H.-C. Nagerl, *Science*, 2008, **321**, 1062–1066.

9 F. Lang, K. Winkler, C. Strauss, R. Grimm and J. H. Denschlag, *Phys. Rev. Lett.*, 2008, **101**, 133005.

10 A. Chotia, B. Neyenhuis, S. A. Moses, B. Yan, J. P. Covey, M. Foss-Feig, A. M. Rey, D. S. Jin and J. Ye, *Phys. Rev. Lett.*, 2012, **108**, 080405.

11 T. Takekoshi, L. Reichsöllner, A. Schindewolf, J. M. Hutson, C. R. Le Sueur, O. Dulieu, F. Ferlaino, R. Grimm and H.-C. Nägerl, *Phys. Rev. Lett.*, 2014, **113**, 205301.

12 P. K. Molony, P. D. Gregory, Z. Ji, B. Lu, M. P. Köppinger, C. R. Le Sueur, C. L. Blackley, J. M. Hutson and S. L. Cornish, *Phys. Rev. Lett.*, 2014, **113**, 255301.

13 J. W. Park, S. A. Will and M. W. Zwierlein, *Phys. Rev. Lett.*, 2015, **114**, 205302.

14 M. Guo, B. Zhu, B. Lu, X. Ye, F. Wang, R. Vexiau, N. Bouloufa-Maafa, G. Quéméner, O. Dulieu and D. Wang, *Phys. Rev. Lett.*, 2016, **116**, 205303.

15 E. B. Norrgard, D. J. McCarron, M. H. Steinecker, M. R. Tarbutt and D. DeMille, *Phys. Rev. Lett.*, 2016, **116**, 063004.

16 A. Prehn, M. Ibrügger, R. Glöckner, G. Rempe and M. Zeppenfeld, *Phys. Rev. Lett.*, 2016, **116**, 063005.

17 J. F. Barry, D. J. McCarron, E. B. Norrgard, M. H. Steinecker and D. DeMille, *Nature*, 2014, **512**, 286–289.

18 S. Truppe, H. J. Williams, M. Hambach, L. Caldwell, N. J. Fitch, E. A. Hinds, B. E. Sauer and M. R. Tarbutt, *Nature Physics*, 2017, **13**, 1173.

19 L. W. Cheuk, L. Anderegg, B. L. Augenbraun, Y. Bao, S. Burchesky, W. Ketterle and J. M. Doyle, *Phys. Rev. Lett.*, 2018, **121**, 083201.

20 A. L. Collopy, S. Ding, Y. Wu, I. A. Finneran, L. Anderegg, B. L. Augenbraun, J. M. Doyle and J. Ye, *Physical Review Letters*, 2018, **121**, 213201.

21 L. De Marco, G. Valtolina, K. Matsuda, W. G. Tobias, J. P. Covey and J. Ye, *arXiv preprint arXiv:1808.00028*, 2018.

22 L. R. Liu, J. D. Hood, Y. Yu, J. T. Zhang, N. R. Hutzler, T. Rosenband and K.-K. Ni, *Science*, 2018, **360**, 900–903.

23 L. Anderegg, L. W. Cheuk, Y. Bao, S. Burchesky, W. Ketterle, K.-K. Ni and J. M. Doyle, *arXiv e-prints*, 2019, arXiv:1902.00497.

24 S. Ospelkaus, K.-K. Ni, D. Wang, M. H. G. de Miranda, B. Neyenhuis, G. Quéméner, P. S. Julienne, J. L. Bohn, D. S. Jin and J. Ye, *Science*, 2010, **327**, 853–857.

25 B. Yan, S. A. Moses, B. Gadway, J. P. Covey, K. R. A. Hazzard, A. M. Rey, D. S. Jin and J. Ye, *Nature*, 2013, **501**, 521–525.

26 B. Gadway and B. Yan, *Journal of Physics B: Atomic, Molecular and Optical Physics*, 2016, **49**, 152002.

27 L. R. Liu, J. T. Zhang, Y. Yu, N. R. Hutzler, Y. Liu, T. Rosenband and K.-K. Ni, *ArXiv:1701.03121*, 2017.

28 N. Schlosser, G. Reymond, I. Protsenko and P. Grangier, *Nature*, 2001, **411**, 1024–7.

29 Y. Miroshnychenko, W. Alt, I. Dotsenko, L. Förster, M. Khudaverdyan, D. Meschede, S. Reick and A. Rauschenbeutel, *Phys. Rev. Lett.*, 2006, **97**, 243003.

30 A. M. Kaufman, B. J. Lester and C. A. Regal, *Phys. Rev. X*, 2012, **2**, 041014.

31 J. D. Thompson, T. G. Tiecke, A. S. Zibrov, V. Vuletić and M. D. Lukin, *Phys. Rev. Lett.*, 2013, **110**, 133001.

32 P. Xu, J. Yang, M. Liu, X. He, Y. Zeng, K. Wang, J. Wang, D. J. Papoular, G. V. Shlyapnikov and M. Zhan, *Nature Communications*, 2015, **6**, 7803.

33 Y. Yu, N. R. Hutzler, J. T. Zhang, L. R. Liu, J. D. Hood, T. Rosenband and K.-K. Ni, *Phys. Rev. A*, 2018, **97**, 063423.

34 J. Deiglmayr, M. Aymar, R. Wester, M. Weidmüller and O. Dulieu, *The Journal of Chemical Physics*, 2008, **129**, 064309.

35 P. J. Dagdigian and L. Wharton, *The Journal of Chemical Physics*, 1972, **57**, 1487–1496.

36 A. Grochola, P. Kowalczyk, J. Szczepkowski, W. Jastrzebski, A. Wakim, P. Zabawa and N. P. Bigelow, *Phys. Rev. A*, 2011, **84**, 012507.

37 A. Wakim, P. Zabawa and N. P. Bigelow, *Phys. Chem. Chem. Phys.*, 2011, **13**, 18887–18892.

38 P. Zabawa, A. Wakim, M. Haruza and N. P. Bigelow, *Phys. Rev. A*, 2011, **84**, 061401.

39 P. S. Żuchowski and J. M. Hutson, *Phys. Rev. A*, 2010, **81**, 060703.

40 X. Ye, M. Guo, M. L. González-Martínez, G. Quéméner and D. Wang, *Science Advances*, 2018, **4**, year.

41 M. Brown, T. Thiele, C. Kiehl, T.-W. Hsu and C. Regal, *arXiv preprint arXiv:1811.01448*, 2018.

42 D. Barredo, S. de Léséleuc, V. Lienhard, T. Lahaye and A. Browaeys, *Science*, 2016, **354**, 1021–1023.

43 M. Endres, H. Bernien, A. Keesling, H. Levine, E. R. Anschuetz, A. Krajenbrink, C. Senko, V. Vuletic, M. Greiner and M. D. Lukin, *Science*, 2016, **354**, 1024–1027.

44 C. Monroe, D. M. Meekhof, B. E. King, S. R. Jefferts, W. M. Itano, D. J. Wineland and P. Gould, *Phys. Rev. Lett.*, 1995, **75**, 4011–4014.

45 X. Li, T. A. Corcovilos, Y. Wang and D. S. Weiss, *Phys. Rev. Lett.*, 2012, **108**, 103001.

46 S. Grishkevich and A. Saenz, *Phys. Rev. A*, 2007, **76**,

022704.

47 R. Wynar, R. S. Freeland, D. J. Han, C. Ryu and D. J. Heinzen, *Science*, 2000, **287**, 1016–1019.

48 T. Rom, T. Best, O. Mandel, A. Widera, M. Greiner, T. W. Hänsch and I. Bloch, *Phys. Rev. Lett.*, 2004, **93**, 073002.

49 C. A. Regal, C. Ticknor, J. L. Bohn and D. S. Jin, *Nature*, 2003, **424**, 47.

50 K. Bergmann, H. Theuer and B. W. Shore, *Rev. Mod. Phys.*, 1998, **70**, 1003–1025.

51 D. Wineland, C. Monroe, W. Itano, D. Leibfried, B. King and D. Meekhof, *Journal of Research of the National Institute of Standards and Technology*, 1998, **103**, 259.

52 A. M. Kaufman, B. J. Lester, C. M. Reynolds, M. L. Wall, M. Foss-Feig, K. R. A. Hazzard, A. M. Rey and C. A. Regal, *Science*, 2014, **345**, 306–309.

53 See supplementary material.

54 K. M. Jones, E. Tiesinga, P. D. Lett and P. S. Julienne, *Reviews of Modern Physics*, 2006, **78**, 483.

55 P. J. Zabawa and N. P. Bigelow, *Ph.D. thesis*, 2012.

56 A. E. Wakim, *Ph.D. thesis*, University of Rochester, 2012.

57 T. A. Savard, K. M. O'Hara and J. E. Thomas, *Phys. Rev. A*, 1997, **56**, R1095.

58 R. Shadmehr and S. Wise, *Supplementary documents for Computational Neurobiology of Reaching and Pointing*, Cambridge, MA: MIT Press, 2005.

59 D. Tannor, *Introduction to Quantum Mechanics*, University Science Books, 2007.

60 M. S. Safronova, B. Arora and C. W. Clark, *Phys. Rev. A*, 2006, **73**, 022505.

61 S. Kallush and R. Kosloff, *Chemical physics letters*, 2006, **433**, 221–227.